Scripta Materialia 203 (2021) 114111

Contents lists available at ScienceDirect

Scripta Materialia

journal homepage: www.elsevier.com/locate/scriptamat

# Factor which governs the feature of texture developed during additive manufacturing; clarified from the study on hexagonal C40-$NbSi_2$

Koji Hagihara[a,b,$,#], Takuya Ishimoto[a,b,#], Masahiro Suzuki[a], Ryosuke Ozasa[a,b], Aira Matsugaki[a,b], Pan Wang[c], Takayoshi Nakano[a,b,*]

[a] Division of Materials and Manufacturing Science, Graduate School of Engineering, Osaka University, 2-1 Yamadaoka, Suita, Osaka 565-0871, Japan
[b] Osaka University Anisotropic Design & AM Research Center, 2-1 Yamadaoka, Suita, Osaka 565-0871, Japan
[c] Singapore Institute of Manufacturing Technology, A*STAR, 73 Nanyang Drive, 637662, Singapore

ARTICLE INFO

*Article history:*
Received 25 March 2021
Revised 13 May 2021
Accepted 21 June 2021
Available online 2 July 2021

*Keywords:*
Transition metal alloys and compounds
Laser processing
Selective laser melting (SLM)
Texture
Electron backscattering diffraction (EBSD)

ABSTRACT

C40-$NbSi_2$ with a hexagonal unit cell is focused as a high-temperature structural material. We first attempted the fabrication of the bulk C40-$NbSi_2$ products via selective laser melting (SLM) in additive manufacturing (AM) process. Strong crystallographic texture control wherein <0001> was parallel to the building direction, i.e. development of the so-called basal fiber texture, was achieved in this study. The texture developed in products does not largely vary by changing the scanning strategy, unlike the textures of $C11_b$-$MoSi_2$ with a tetragonal unit cell and a $\beta$-Ti alloy with a cubic unit cell. A comparison of these results led us to the conclusion that crystal symmetry, i.e., the multiplicity of the preferential crystal growth direction, is one of the primary factors that governs the features of the textures developed in AM-built materials.



The application of transition-metal disilicides (TMDs) as ultrahigh-temperature structural materials has become an area of interest owing to their high melting temperatures, superior oxidation resistance, low density, and high thermal conductivity [1–5]. $MoSi_2$, which crystallizes in the tetragonal $C11_b$-structure, is the most promising candidate because it can undergo plastic deformation by employing several slip systems [4, 5]. TMDs with hexagonal C40 structures are also focused in structural applications [3, 6]. $NbSi_2$ is the most promising C40 disilicide in terms of melting points, densities, and the occurrence of yield stress anomalies at high temperatures of approximately 1400°C [6]. In addition, a dual-phase C40-$NbSi_2$/$C11_b$-$MoSi_2$ crystal with oriented lamellar microstructure was recently developed by using the single-phase (Mo, Nb)$Si_2$ C40 single-crystal as the starting material. The C40/$C11_b$ lamellar microstructure drastically improved the fracture toughness and high-temperature strength of the crystal [7–14].

However, the low workability of the TMDs at low temperatures prevents their application in the fabrication of commercial products. Additive manufacturing (AM) is being studied as a novel fabrication process to address this limitation. AM can be used to fabricate products with complex geometries that cannot be fabricated with standard manufacturing techniques, such as casting and forming, even for high-temperature structural materials with brittleness at room temperature [15-24]. Although there had been no reports of the fabrication of TMD products by AM processes, we recently succeeded to making the $MoSi_2$ product by selective laser melting (SLM) [25]. On the basis of this knowledge, SLM was attempted for $NbSi_2$. This study first discusses the fabrication of an $NbSi_2$ product through AM, followed by an analysis of the factor that governs the developing feature of the texture of AM-built materials. Emphasis was placed on the crystal symmetry in these materials.

For the fabrication of AM-products, a pre-alloyed ingot was pulverized to obtain a powder with an average diameter of ~27 $\mu$m. This powder was used to manufacture 10 mm × 10 mm × 10 mm cubic samples with an SLM device in an argon atmosphere. In fabrication, three different strategies of beam scan; bidirectional (zigzag) one direction scanning (X-scan), bidirectional scanning with a rotation angle of 90° for each layer (XY-scan), and rotational scanning with a rotation angle of 67° (Rot-scan) were performed. Further detailed parameters in SLM and experimental methods are described in “Supplementary information” file.

As the experimental result, the process map for fabrication of $NbSi_2$ samples by varying the scanning speed in the X-scan strategy is displayed in Fig. 1. Products with desired shapes can be fab-

* Corresponding author.
*E-mail address:* nakano@mat.eng.osaka-u.ac.jp (T. Nakano).
$ Present address: Department of Physical Science and Engineering, Nagoya Institute of Technology, Gokiso, Nagoya 466-8555, Japan
# The authors equally contributed to this study: Koji Hagihara, Takuya Ishimoto

https://doi.org/10.1016/j.scriptamat.2021.114111

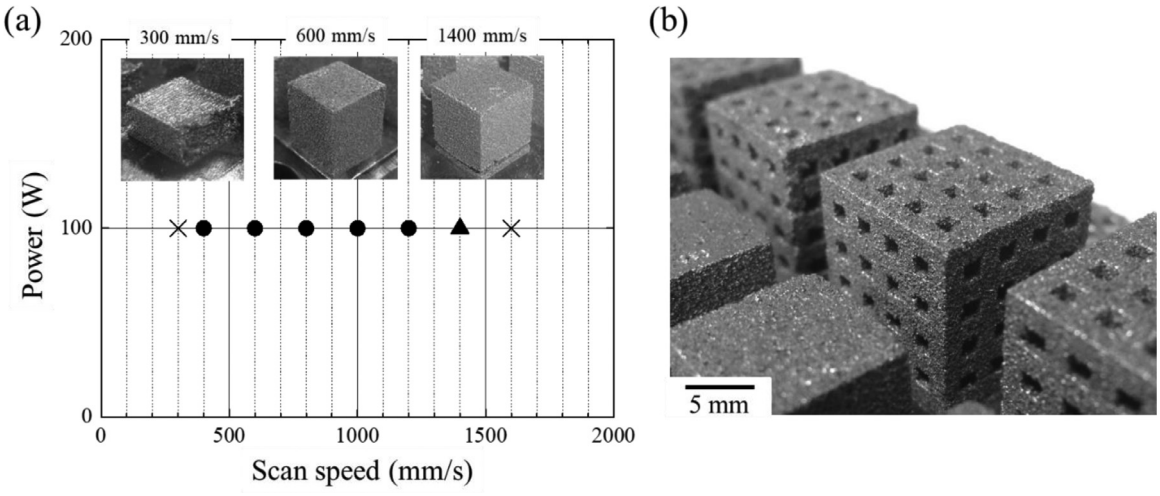


**Fig. 1.** (a) Process map indicating the availability of $NbSi_2$ products by varying the scanning speed in SLM. (b) Appearance of jungle gym-shaped products fabricated at 800 mm/s.

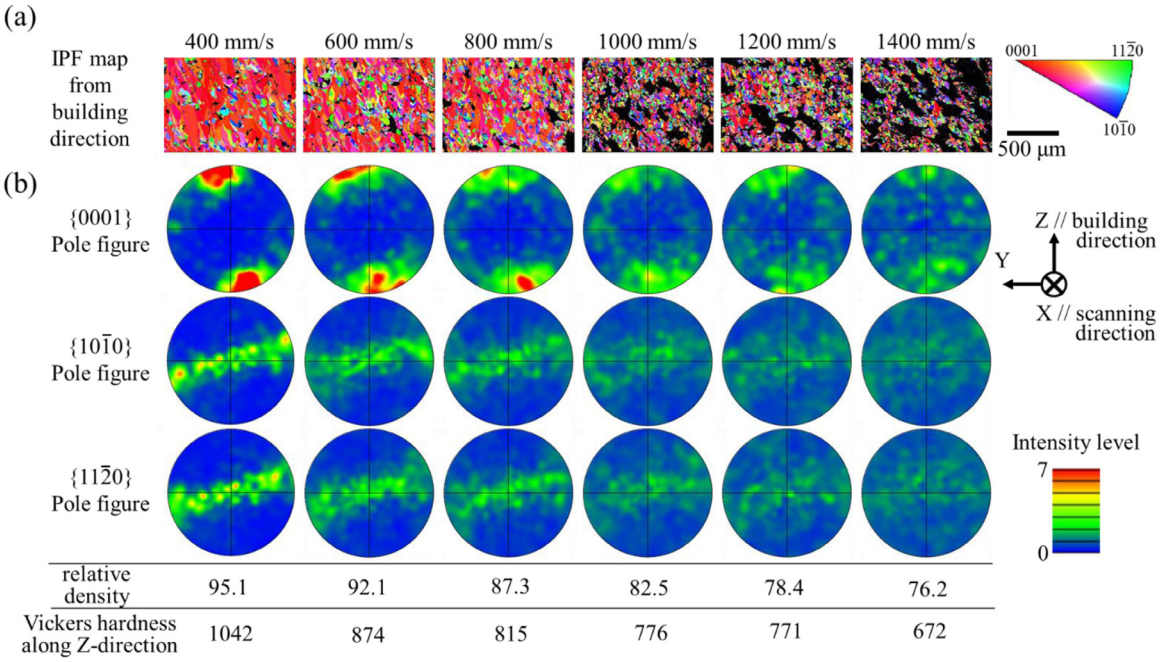


**Fig. 2.** (a) Variation in the crystal orientation maps of the $NbSi_2$ samples fabricated with the X-scan strategy with the scanning speed. The observation was conducted on the plane perpendicular to the scanning direction (X-cross-section), but the colors of the grains indicate the crystallographic orientation along the building Z-direction. (b) Corresponding {0001}, {10$\bar{1}$0}, and {11$\bar{2}$0} pole figures for each sample. The relative density of the samples measured by Archimedes' method and the Vickers hardness value measured along the Z-building direction in samples are also indicated.

ricated at scanning speeds varying from 400 to 1400 mm/s, although the partial occurrence of cleavage between the accumulated layers was observed at 1400 mm/s due to insufficient melting, which was attributed to less input energy density. At the appropriate scanning speed, complicated jungle gym-shaped products could be prepared as shown in Fig. 1(b).

Fig. 2(a) shows the variation in the crystal orientation map with the scanning speed in the X-scan samples. Fig. 2(b) shows the corresponding {0001}, {10$\bar{1}$0}, and {11$\bar{2}$0} pole figures. Note that although the observation was conducted in a plane perpendicular to the scanning direction (X-cross-section), the colors of the grains indicates the crystallographic orientation along the building Z-direction in Fig. 2(a). The bulk product could be manufactured under varying operating conditions; however, the properties of the product were largely dependent on the scanning speed. In the 1400 mm/s sample, the apparent density measured by Archimedes' method was as low as ~76%, and there were large amounts of voids shown in black in Fig. 2(a). However, the number of voids decreased drastically with the decreasing scanning speed. Consequently, the apparent density of the product increased rapidly, reaching ~95% of the apparent density of 400 mm/s sample. A more complete reduction of voids is desired for practical use, but these results suggest that this is expected to be achieved by further adjustment of process parameters for manufacturing.

The variation in apparent density of the sample affected their strength. In the measurement of Vickers hardness along the Z-building direction, the hardness was monotonically increased as decreasing the scanning speed as indicated in Fig. 2. This suggests the importance of the reduction of voids.

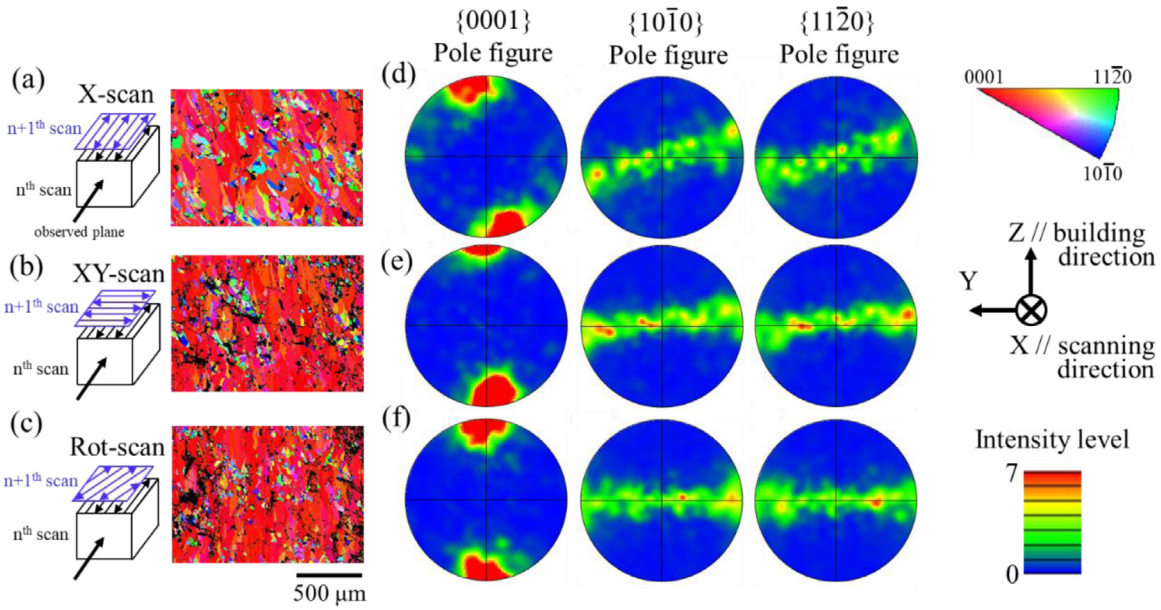


**Fig. 3.** (a–c) Crystal orientation maps of the samples fabricated by the (a) X-scan, (b) XY-scan, and (c) Rot-scan strategies. The observation directions of samples are parallel to the X-direction, i.e., parallel to the scanning direction for the X-scan strategy and perpendicular to the building direction, and the colors of the grains indicates the crystallographic orientation along the Z-direction, as well as that in Fig. 2(a). (d–f) Corresponding {0001}, {10$\bar{1}$0}, and {11$\bar{2}$0} pole figures for Fig. 2(a–c).

Interestingly, the reduction in the apparent density changed the crystallographic textures of the products. The intensity of the {0001} in the 400 mm/s sample was strongly concentrated along the building direction although being slightly inclined at ~10° in the Y-direction. In contrast, no spot-like concentration of intensity was observed in the {10$\bar{1}$0} and {11$\bar{2}$0} pole figures. The intensity profile was band-like and nearly perpendicular to the building direction. The pole figures demonstrate that strong "fiber-like texture," wherein the {0001} was parallel to the building direction, was developed in the X-scan product at a low scanning speed. To compare the obtained results, a $NbSi_2$ single crystal was prepared by optical floating zone method, and the Vickers hardness along [0001] was evaluated as 784 Hv. This demonstrates the appropriate texture control and reduction of voids can realize the comparable or somewhat higher Vickers hardness in SLM samples than that in the single crystal. Higher hardness may be ascribed to the introduction of dislocations and low angle grain boundaries in the SLM samples. It was previously clarified that the (0001)<11$\bar{2}$0> basal slip is the predominant operative deformation mode in C40-$NbSi_2$ in the wide temperature range between 20~1700°C [6]. Thus, the <0001> basal-fiber texture in AM-built $NbSi_2$ products is significantly desirable to ensure the superior strength not only at room temperature but also at high-temperatures, since the Schmid factor for basal slip becomes negligible when the stress acts parallel to the building direction. The effectiveness of the suppression of basal slip for improving the high-temperature creep property was indeed confirmed in a previous study by using single crystals [14].

The development of the <0001> fiber texture weakened with increasing scanning speed, which was similar to the trend observed in the AM-built $MoSi_2$ product [25]. The rise in the scanning speed increased the number of voids formed in the samples due to a lack of sufficient energy input to melt the powder, as shown in Fig. 2(a). The voids disturbed the epitaxial growth of the grains beyond the melt pool boundary and weakened the texture.

Several studies have reported that the texture can be varied by controlling the scanning strategy during the AM process in cubic-symmetry materials [26-32]. However, the information for hexagonal material was few available, thus this study attempts to focus on them. Figs. 3(a–c) show a comparison between the crystal orientation maps of the samples fabricated by the X-scan, XY-scan, and Rot-scan strategies, respectively. The corresponding {0001}, {10$\bar{1}$0}, and {11$\bar{2}$0} pole figures are displayed in Figs. 3(d–f). A similar <0001> fiber texture was developed in all samples. This indicated that the variation in the texture with the scanning strategy was negligible, unlike the observations made in previous studies for cubic-symmetry materials [26-32].

The development mechanism of the texture of the $NbSi_2$ product was studied through microstructural observations. Figs. 4(a) and 4(b) show an optical micrograph of the X-scan sample along the X-scanning direction and the corresponding crystal orientation map, respectively. Traces of the melt pool with a half-ellipse shape were observed in the X-cross-section, as shown in Fig. 4(a). The columnar cells in the melt pool elongate approximately along the building direction, i.e. close to the direction of maximum thermal gradient, although small disturbances exist. When observed the solidification microstructure on the Y-cross-section (Fig. 4(c)), on the other hand, the elongation directions of the cells were almost parallel to the building direction. The deviation angles in this case were smaller than those observed in the X-cross-section (Fig. 4(a)). These results demonstrate that samples with strong texture reported the preferential growth of cells in a plane perpendicular to the X-scanning direction and their elongation approximately along the building direction. These results are consistent with those of previous studies on $MoSi_2$ and $\beta$-Ti [25, 31].

Furthermore, the <0001> direction in each grain was examined from Fig. 4(b), and displayed by red arrows in Fig. 4(a). The <0001> direction in each grain was almost coincident with the elongation direction of the cells, i.e., the columnar cells in the $NbSi_2$ sample were elongated along <0001> in most of the melt pool. This observation is consistent with a previous study that reported that the preferential grain growth direction in the $NbSi_2$ sample was parallel to <0001> [33].

It is noteworthy that the sizes of the grains, i.e., regions with similar crystal orientations in the crystal orientation map (Fig. 4(b)), were larger than the columnar cells in the melt pools. This indicates that the same crystal orientation extended beyond the melt-pool boundaries in several regions. This strongly suggests that the preferential growth of the columnar cells along <0001>

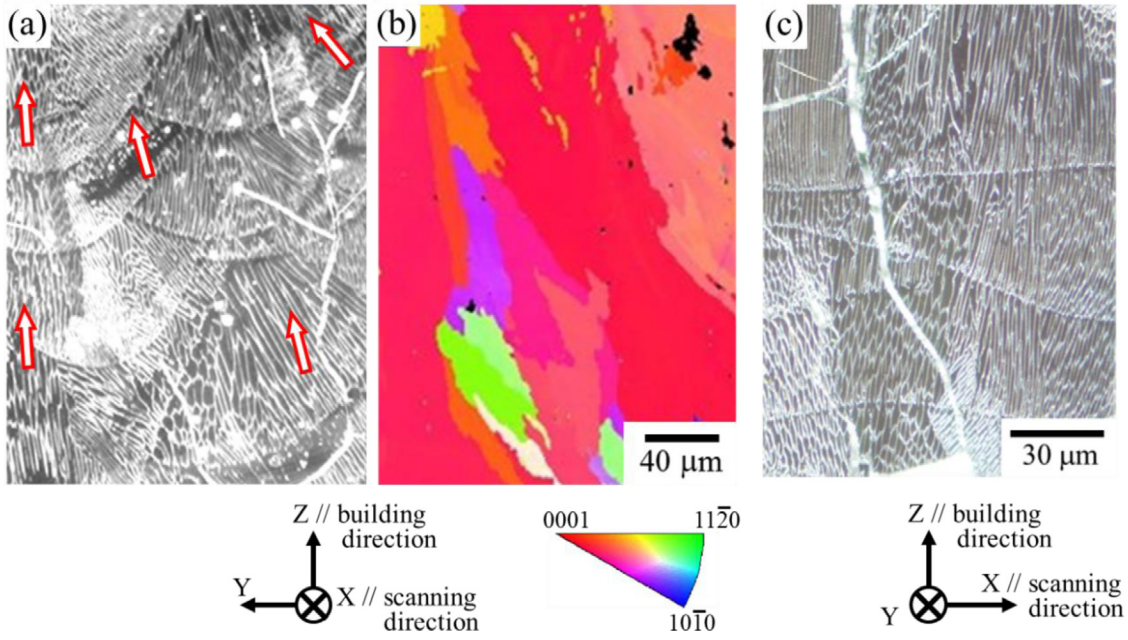


**Fig. 4.** OM images showing the morphology of the elongated cells in the melt-pools of the sample fabricated by the X-scan strategy at a scanning speed of 400 mm/s. (a) OM image of the X-cross-section and (b) the corresponding crystal orientation map. The colors of the grains indicate the crystallographic orientation along the Z-direction.(c) OM image observed on the Y-cross-section.

and their epitaxial growth beyond the melt pool boundary are the origins of the development of the <0001> basal-fiber texture along the building direction through the formation of largely elongated grains.

The report on texture formation behavior in hexagonal crystals during AM processes is limited [34], other than the present study. The variation in texture with scan strategy has not been studied, and therefore factors governing the development of texture dependent on scan strategy is not sufficiently clarified yet. Interestingly, the crystallographic features of the texture of the $NbSi_2$ sample were different from those of the textures of the tetragonal $MoSi_2$ [25] and body-centered cubic (bcc) $\beta$-Ti [31]. A comparison of the texture-developing mechanisms in these materials indicated that the crystal symmetry of the unit cell in the material, as shown in Fig. 5(a), strongly governs the crystallographic features of the texture developed during the AM process.

According to previous studies, the single-crystalline texture can be developed in AM-built bcc materials, such as $\beta$-Ti, and face-centered cubic (fcc) materials, such as Ni-based superalloys, by choosing the appropriate process parameters [26–32]. But the crystallographic nature is varied depending on the scanning strategy [26–32]. <100> and <011> are aligned along the scanning and building directions, respectively, in the X-scan strategy. However, the aligned direction along the building direction is changed to <001> in the XY-scan strategy [29, 31]. The mechanism of these texture variation has been discussed in previous studies [31]. The preferential growth direction of the elongated cell in the melt pool is parallel to <100> in most fcc and bcc materials, and the cells elongate at 45° with respect to the building direction in the X-scan samples [29,31,35,36]. This is because the primary and secondary elongation directions of the cell on both sides of the melt pool tend to maintain the <100> direction during the solidification process to facilitate the epitaxial growth [31]. Thus, a single-crystalline texture wherein <011> is parallel to the building direction is developed, as shown in Fig. 5(b). However, in the case of the XY-scan, the cells elongate along the building direction in the melt pool in the X-scan and the following Y-scan to maintain an identical crystal orientation in both scan regions [31]. As a result, a single-crystalline texture that is 45° rotated with respect to the texture developed in the X-scan sample, i.e., the texture in which the building direction is parallel to <001> is developed [29, 31].

A similar texture development mechanism was observed in the $C11_b$-$MoSi_2$ sample; however, the crystallographic features of this texture were slightly different from those of the textures observed in the fcc and bcc metals, due to the decrease in crystal symmetry. The $C11_b$ structure in $MoSi_2$ has a tetragonal unit cell wherein three bcc lattices are stacked along the *c*-axis (Fig. 5(a)). The preferential growth direction of the elongated cells in $MoSi_2$ was reported to be parallel to <100] [25]. Note that, in $MoSi_2$ the mixed notation of {*hkl*) and <*uvw*], which differentiates the first two indices from the third index that does not play the same role as the first two, is used because of the tetragonality of the $C11_b$ crystal structure. It was found that the growth of the columnar cells primarily occurs in the plane perpendicular to the scanning direction in samples with strong texture, as similarly to the fcc and bcc materials. Thus, in case of the X-scan, the preferential growth of the cells parallel to <100] and the subsequent lateral growth parallel to <010] tend to occur on the X-cross-section, because the [100] and [010] directions are crystallographically equivalent in the tetragonal crystal. As a result, [001], which is perpendicular to both [100] and [010], is aligned along the X-scanning direction. Thus, a single-crystalline texture is developed [25], as similarly to fcc and bcc materials.

In case of XY-scan in $MoSi_2$, however, it was impossible to match the crystal orientations in the X-scan and Y-scan regions, unlike the cases in the fcc and bcc materials. This is because the *a*-axis and *c*-axis are not crystallographically equivalent in the tetragonal $C11_b$-$MoSi_2$ (Fig. 5(a)). Thus, a single-crystalline texture could not be developed for $C11_b$-$MoSi_2$ through the XY-scan, and only a weak fiber texture, wherein <100] was parallel to the building direction, was developed in the XY-scan sample [25].

Contrary to those results, a single-crystalline texture could not be developed through any scanning strategy for hexagonal C40-$NbSi_2$. The preferred cell growth direction for $NbSi_2$ was found to be <0001>. Note here that the <0001> is only “one” direction in the unit cell of the hexagonal crystal. This differs from the <100> in cubic materials wherein the “three” directions are parallel to <100>. Further, this also differs from the <100] in the tetragonal

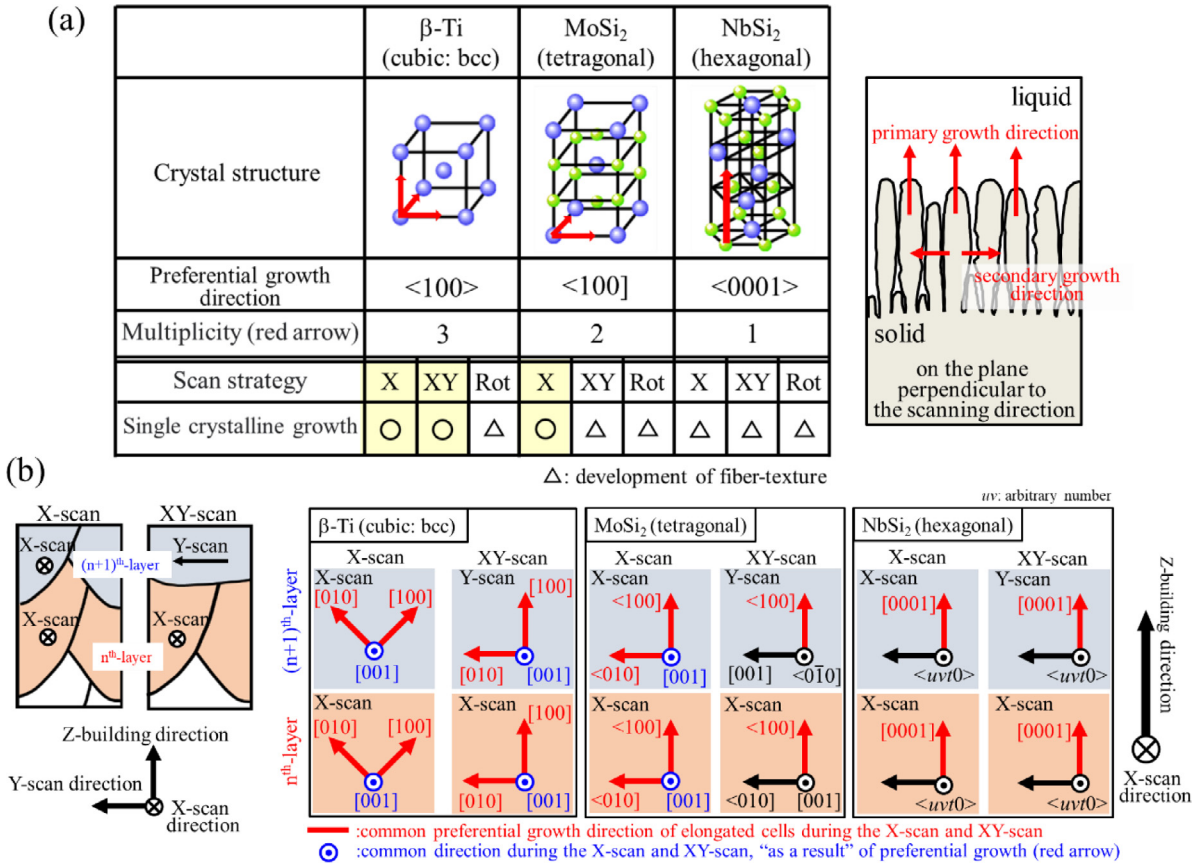


**Fig. 5.** (a) Relationship between the crystal structure, preferential growth direction of the elongated cell, and the texture developed in the SLM process. (b) Schematic of the variations in the developing features of the texture with crystal structures during the X-scan and XY-scan processes.

$C11_b$-$MoSi_2$ wherein "two" directions are parallel to the <100] in the unit cells, denoted by "multiplicity" in Fig. 5(a) with red arrows. Thus, during the growth process of the elongated cells in $NbSi_2$, the primary elongation direction was parallel to <0001>, but the subsequent lateral growth (secondary growth) direction in the X-cross-section was arbitrary because only one <0001> axis existed in the hexagonal crystal. This is the reason behind the absence of a single-crystalline texture and the development of a fiber-like texture wherein only <0001> is parallel to the building direction, and the X-scanning direction is expressed as <*uvt*0>, where *u* and *v* are arbitrary numbers and $t = -(u+v)$. The situation is not changed in any scanning strategies. Thus, no significant changes were observed in the textures of the samples.

As a conclusion, we have first obtained the $NbSi_2$ samples fabricated via SLM, by tuning-up the appropriate process parameters. It was observed that a fiber-like texture, wherein <0001> was aligned along the building direction, could be developed with all scanning strategies, thereby improving the strength of the product. A comparison of the results of the cubic fcc and bcc materials and tetragonal $C11_b$-$MoSi_2$ confirmed that the crystal symmetry in the material, i.e., the multiplicity of the preferential growth direction of the cells, is an essential factor that governs the development of the textures in AM processes. This study can provide new insight into the texture control through additive manufacturing.

## Declaration of Competing Interest

The authors declare that they have no known competing financial interests or personal relationships that could have appeared to influence the work reported in this paper.

## Acknowledgement

Funding: This work was supported by Grants-in-Aid for Scientific Research (JP18H05254) from the Japan Society for the Promotion of Science (JSPS). This work was also partly supported by the Cross-Ministerial Strategic Innovation Promotion Program (SIP), Materials Integration for Revolutionary Design System of Structural Materials, Domain C1: "Development of Additive Manufacturing Process for Ni-based Alloy" from the Japan Science and Technology Agency (JST).

## Supplementary materials

Supplementary material associated with this article can be found, in the online version, at doi:10.1016/j.scriptamat.2021.114111.

## References

[1] Y. Umakoshi, T. Sakagami, T. Hirano, T. Yamane, Acta Metall. Mater. 38 (1990) 909–915.
[2] A.K. Vasudévan, J.J. Petrovic, Mater. Sci. Eng. A 155 (1992) 1–17.
[3] W.J. Boettinger, J.H. Perepezko, P.S. Frankwicz, Mater. Sci. Eng. A 155 (1992) 33–44.
[4] K. Ito, H. Inui, Y. Shirai, M. Yamaguchi, Philos. Mag. A 72 (1995) 1075–1097.
[5] K. Ito, T. Yano, T. Nakamoto, M. Moriwaki, H. Inui, M. Yamaguchi, Prog. Mater. Sci. 42 (1997) 193–207.
[6] T. Nakano, M. Kishimoto, D. Furuta, Y. Umakoshi, Acta Mater. 48 (2000) 3465–3475.
[7] T. Nakano, M. Azuma, Y. Umakoshi, Intermetallics 6 (1998) 715–722.
[8] F.G. Wei, Y. Kimura, Y. Mishima, Intermetallics 9 (2001) 661–670.
[9] T. Nakano, Y. Nakai, S. Maeda, Y. Umakoshi, Acta Mater. 50 (2002) 1781–1795.
[10] T. Nakano, K. Hagihara, Y. Nakai, Y. Umakoshi, Intermetallics 14 (2006) 1345–1350.
[11] Y. Kimura, M. Komiyama, Y. Mishima, Intermetallics 14 (2006) 1358–1363.
[12] K. Hagihara, T. Nakano, Acta Mater. 59 (2011) 4168–4176.

[13] K. Hagihara, Y. Hama, K. Yuge, T. Nakano, Acta Mater. 61 (2013) 3432–3444.
[14] K. Hagihara, H. Araki, T. Ikenishi, T. Nakano, Acta Mater. 107 (2016) 196–212.
[15] D. Wang, Z. Wang, K. Li, J. Ma, W. Liu, Z. Shen, Mater. Des. 162 (2019) 384–393.
[16] O. Gokcekaya, N. Hayashi, T. Ishimoto, K. Ueda, T. Narushima, T. Nakano, Addit. Manuf. (2020) 101624.
[17] O. Gokcekaya, T. Ishimoto, T. Todo, R. Suganuma, R. Fukushima, T. Narushima, T. Nakano, Crystals 11 (2021) 9.
[18] M. Higashi, T. Ozaki, Mater. Des. 191 (2020) 108588.
[19] L. Thijs, M.L. Montero Sistiaga, R. Wauthle, Q. Xie, J.-P. Kruth, J. Van Humbeeck, Acta Mater. 61 (2013) 4657–4668.
[20] J. Yang, X. Jin, H. Gao, D. Zhang, H. Chen, S. Zhang, X. Li, Mater. Charact. 170 (2020) 110694.
[21] C. Tan, K. Zhou, W. Ma, B. Attard, P. Zhang, T. Kuang, Sci. Technol. Adv. Mater. 19 (2018) 370–380.
[22] A.V. Müller, G. Schlick, R. Neu, C. Anstätt, T. Klimkait, J. Lee, B. Pascher, M. Schmitt, C. Seidel, Nucl. Mater. Energy 19 (2019) 184–188.
[23] Z. Xiong, P. Zhang, C. Tan, D. Dong, W. Ma, K. Yu, Adv. Eng. Mater. 22 (2020) 1901352.
[24] Z. Hu, Y. Zhao, K. Guan, Z. Wang, Z. Ma, Addit. Manuf. 36 (2020) 101579.
[25] K. Hagihara, T. Nakano, M. Suzuki, T. Ishimoto, S.-H. Suyalatu, S. Sun, J. Alloys Compd. 696 (2017) 67–72.
[26] T. Ishimoto, S. Wu, Y. Ito, S.-H. Sun, H. Amano, T. Nakano, ISIJ Int. 60 (2020) 1758–1764.
[27] J.J. Marattukalam, D. Karlsson, V. Pacheco, P. Beran, U. Wiklund, U. Jansson, B. Hjörvarsson, M. Sahlberg, Mater. Des. 193 (2020) 108852.
[28] F. Geiger, K. Kunze, T. Etter, Mater. Sci. Eng. A 661 (2016) 240–246.
[29] S.-H. Sun, K. Hagihara, T. Nakano, Mater. Des. 140 (2018) 307–316.
[30] L. Thijs, K. Kempen, J.P. Kruth, J.V. Van Humbeeck, Acta Mater. 61 (2013) 1809–1819.
[31] T. Ishimoto, K. Hagihara, K. Hisamoto, S.-H. Sun, T. Nakano, Scr. Mater. 132 (2017) 34–38.
[32] T. Ishimoto, K. Hagihara, K. Hisamoto, T. Nakano, Addit. Manuf. 43 (2021) 102004 in press.
[33] S. Fujio, K. Tanaka, H. Inui, Intermetallics 15 (2007) 245–252.
[34] M. Esmaily, Z. Zeng, A.N. Mortazavi, A. Gullino, S. Choudhary, T. Derra, F. Benn, F. D'Elia, M. Müther, S. Thomas, A. Huang, A. Allanore, A. Kopp, N. Birbilis, Addit. Manuf. 35 (2020) 101321.
[35] S.-H. Sun, T. Ishimoto, K. Hagihara, Y. Tsutsumi, T. Hanawa, T. Nakano, Scr. Mater. 159 (2019) 89–93.
[36] O. Gokcekaya, T. Ishimoto, S. Hibino, J. Yasutomi, T. Narushima, T. Nakano, Acta Mater. 212 (2021) 116876.